

Cite this: *Chem. Sci.*, 2019, 10, 6382

All publication charges for this article have been paid for by the Royal Society of Chemistry

# Under-liquid dual superlyophobic nanofibrous polymer membranes achieved by coating thin-film composites: a design principle†

Qifei Wang, <sup>a</sup> Yang Wang, <sup>b</sup> Baixian Wang, <sup>a</sup> Zhiqiang Liang, <sup>a</sup> Jiancheng Di <sup>\*a</sup> and Jihong Yu <sup>\*ac</sup>

Surfaces with under-liquid dual superlyophobicity have garnered tremendous interest because of their promising applications, but their unexplored underlying nature restricts the designed construction of such surfaces. Herein, we coated the thin-film composites with different terminal groups over the electrospun polyacrylonitrile nanofibrous membranes, which afforded the membranes excellent stability in organic solvents, as well as modulated under-liquid wetting behaviors. Among them, the representative under-liquid dual superlyophobic 4-cyan-Ph-terminated membrane could realize highly efficient separation of all types of oil/water mixtures and even emulsions. Moreover, we found that the under-liquid wetting behaviors could be classified in terms of the intrinsic water contact angle ( $\theta_w$ ). By comparing the total interfacial energy, we proved that the under-liquid dual lyophobic surfaces were thermodynamically metastable. On this basis, we could predict the  $\theta_w$  of rough surfaces with the under-liquid dual lyophobicity in a given oil–water–solid system (e.g., 47.3–89.1° in cyclohexane–water–solid system,  $R = 2$ ). This work provides a design principle for the fabrication of under-liquid dual superlyophobic surfaces, which will open potential applications in diverse fields in terms of such smart surfaces.

Received 2nd April 2019

Accepted 20th May 2019

DOI: 10.1039/c9sc01607d

rsc.li/chemical-science

## 1. Introduction

Surfaces with special wetting behaviors have garnered considerable attention for their versatile applications in a broad range of fields.<sup>1–7</sup> For instance, surfaces inspired by nature with superhydrophobicity/superoleophilicity in air (lotus leaves)<sup>8,9</sup> or superhydrophilicity/under-water superoleophobicity (fish scales)<sup>10,11</sup> have been evidenced as eligible candidates that can selectively remove oils or water from oil/water mixtures. Compared with the surfaces that possess irreversible wetting behaviors, smart surfaces are more attractive because their wetting behaviors can be switched when stimulated by light,<sup>12,13</sup> pH,<sup>14</sup> temperature,<sup>15,16</sup> electricity,<sup>17</sup> etc. As a result, these surfaces are of great significance for various applications, such as in liquid transfer systems, microdroplet reactors, selective oil/water separating units, and so on.<sup>18–21</sup>

Recently, several intriguing surfaces with switchable oil–water repellency simply triggered by the prewetted liquids have been reported, which exhibit superoleophobicity and superhydrophobicity when immersed in water and oil, respectively.<sup>22–27</sup> However, the rational construction of surfaces with under-liquid dual superlyophobicity remains challenging due to the lack of a design principle. Notably, Tian and coworkers proposed that the under-liquid dual lyophobic surfaces could be obtained on the re-entrant structured silicon wafer with their intrinsic water contact angle ( $\theta_w$ ) ranging from 56° to 74°. <sup>28</sup> Meanwhile, the authors suggested that a thermodynamically stable surface should have strong affinity to either water or oil, showing under-water oleophobicity/under-oil hydrophilicity or under-water oleophilicity/under-oil hydrophobicity. The under-oil water contact angle ( $\theta_{w/o}$ ) and under-water oil contact angle ( $\theta_{o/w}$ ) on such surface were supplementary to each other and the sum of them should be up to 180°. Thus, the under-liquid dual lyophobic surfaces with both  $\theta_{w/o}$  and  $\theta_{o/w}$  larger than 90° might be thermodynamically metastable. However, the underlying nature of the under-liquid wetting behaviors has not yet been investigated in terms of the thermodynamic wetting models. In addition, the prerequisite for this work is based on the specific re-entrant topology, which may not provide a general guidance for the fabrication of under-liquid dual lyophobic surfaces with various geometries.

<sup>a</sup>State Key Laboratory of Inorganic Synthesis and Preparative Chemistry, College of Chemistry, Jilin University, Changchun 130012, P. R. China. E-mail: jcdi@jlu.edu.cn; jihong@jlu.edu.cn

<sup>b</sup>Department of Mechanical Engineering, City University of Hong Kong, 83rd Tat Chee Avenue, Kowloon, Hong Kong

<sup>c</sup>International Center of Future Science, Jilin University, Changchun 130012, P. R. China

† Electronic supplementary information (ESI) available. See DOI: 10.1039/c9sc01607d



As is well-known that the wetting behaviors on the rough surface can be reflected by the apparent contact angles, which are determined by the surface geometries<sup>25,29,30</sup> and the chemical compositions.<sup>28,31,32</sup> For instance, in the Wenzel wetting model (the liquid fully permeates and wets the surface), the lyophilicity or lyophobicity of surfaces with intrinsic contact angle smaller or larger than 90° can be enhanced with the increase of the surface roughness.<sup>33–36</sup> Moreover, the systematic modulation of the wetting behaviors can be achieved by altering the chemical compositions of the surface with a specific topography. Polyacrylonitrile (PAN) is a commercial polymer that can be shaped into fibrous membranes simply by electrospinning technique owing to its excellent viscoelasticity and high mechanical strength.<sup>37–39</sup> Furthermore, the abundant cyano-groups can facilitate the surface modification of PAN membranes *via* a simple coating process, affording them unique properties.<sup>40</sup> For example, in the applications of nano-filtration and reverse osmosis, the PAN membranes are often modified by the thin-film composites to increase their stability in the aprotic solvents like dimethylformamide (DMF) and dimethyl sulfoxide (DMSO).<sup>41</sup> More importantly, the surface chemical compositions of the coated thin-film composites can be easily adjusted by changing the coating agents with different terminal groups.<sup>42</sup>

In this work, thin-film composites (TFs) with different terminal groups were coated over the electrospun PAN nanofibers, giving rise to different surface wetting behaviors of the resultant membranes (TFPNMs): (1) under-water oleophobicity/under-oil hydrophilicity, (2) under-water oleophilicity/under-oil hydrophobicity, and (3) under-liquid dual lyophobicity. Among these, the representative 4-cyan-Ph-terminated TFPNM (CTFPNM) with under-liquid dual superlyophobicity showed high mechanical strength and excellent stability in organic solvents, which could achieve highly efficient separation of arbitrary oil/water mixtures, even surfactant-stabilized oil-in-water and water-in-oil emulsions. Furthermore, in terms of thermodynamic wetting models, we proved that the under-liquid dual lyophobic surfaces were thermodynamically metastable, whereas the surfaces with the other two under-liquid wetting behaviors were thermodynamically stable. Significantly, when using the intrinsic water contact angle ( $\theta_w$ ) of surface as a variable, the  $\theta_w$  regions that corresponded to the three under-liquid wetting behaviors on the rough surfaces in a given oil–water–solid system could be predicted, which well covered the experimental data.

## 2. Results and discussion

### 2.1 Fabrication of polyacrylonitrile nanofibrous membranes coated with thin-film composites

The polyacrylonitrile (PAN) nanofibrous membranes (PNMs) coated by the thin-film composites (TFs) were fabricated as illustrated in Fig. 1a, and the resultant membranes were named as TFPNMs. Typically, a TF was coated over the electrospun PAN nanofibers (compound 1 in Fig. 1a) by using 1,4-dicyanobenzene (compound 2 in Fig. 1a) through an interfacial polymerization process, resulting in 4-cyan-Ph-terminated PAN

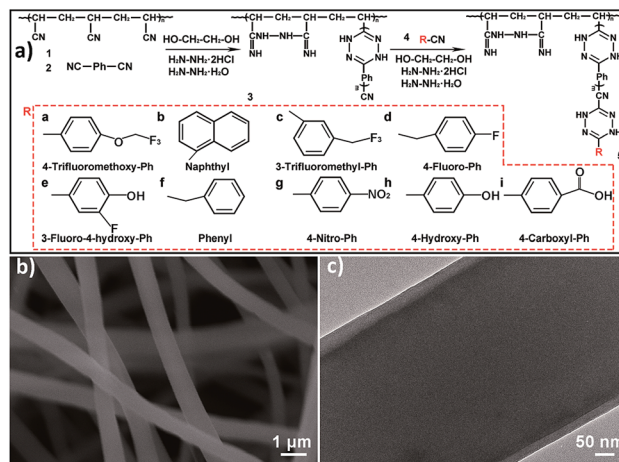


Fig. 1 The fabrication of thin-film composites coated PAN nanofibrous membranes. (a) General routes of the synthesis of TFPNs with different terminal groups. (b) SEM image of CTFPNs. (c) TEM image of CTFPN, showing the core–shell structure of the nanofiber.

nanofibers (CTFPNs, compound 3 in Fig. 1a). The further modification was conducted by grafting nitriles with different terminal groups (compound 4 in Fig. 1a and Table S1†) on CTFPNs, thus affording the modulation of the surface chemical compositions of the TF coated PAN nanofibers (TFPNs, compound 5 in Fig. 1a). The scanning electron microscopy (SEM) image in Fig. S1a† reveals the PNM is composed of intertwined PAN nanofibers. As seen in Fig. S2a,† the diameters of these fibers distribute in a wide range from 400 to 900 nm (mainly in 700–800 nm). After the coating of 4-cyan-Ph-terminated TF, the CTFPNs maintain the fibrous morphology, but the average fiber diameter increases by around 100 nm compared with that of PAN fibers (Fig. 1b and Fig. S2b†). The transmission electron microscopy (TEM) image in Fig. 1c clearly displays the core–shell structure of a CTFPN, proving the successful formation of 4-cyan-Ph-terminated TF over the PAN nanofibers. Fig. S1b–k† exhibits the morphologies of the TFPNs with different terminal groups. Compared with the CTFPNs, there are no changes on the fiber diameters of the TFPNs. Fig. S3† shows the tensile stress vs. strain curves of PNM and 4-cyan-Ph-terminated TFPNM (CTFPNM). The derived Young's modulus and stress of break of CTFPNM are close to those of PNM, suggesting that the coated TF will not significantly decrease the mechanical strength of the membrane.

FT-IR spectra were employed to characterize the chemical structure of CTFPNM (Fig. S4†). In the spectrum of CTFPNM, the intensity of characteristic absorption peak at 2250 cm<sup>−1</sup> that corresponds to the C≡N stretching vibration decreases, which is attributed to the polymerization between the terminal cyano-group and hydrazine hydrate.<sup>40</sup> The new absorption peak appeared at 1580 cm<sup>−1</sup> is assigned to the benzene ring.<sup>43</sup> The broad adsorption peaks located in the region of 1080–1640 cm<sup>−1</sup> correspond to the stretching vibrations of C=N (1634 cm<sup>−1</sup>) and N–N (1100 cm<sup>−1</sup>), mixed C–N stretching and N–H bending vibrations (1200–1350 cm<sup>−1</sup>).<sup>40,41</sup> The other peaks in this region (1460 cm<sup>−1</sup> and 2920 cm<sup>−1</sup>) correspond to the



C–H band of alkane groups.<sup>40</sup> These data illustrate the formation of cyclic nitrogen-containing structures, which further confirm the successful modification of 4-cyan-Ph-terminated thin-film composites on PNM.<sup>41</sup> Note that, we cannot distinguish the characteristic peaks of the terminal groups of other TFPNMs from the FT-IR spectra because these signals are too weak. To ascertain the existence of TFs on CTFPNMs after the coating process, four representative TFPNMs containing F element (4-trifluoromethoxy-Ph-, 3-trifluoromethyl-Ph-, 4-fluoro-Ph-, and 3-fluoro-4-hydroxy-Ph-TFPNM) were characterized by X-ray photoelectron spectroscopy measurement. In Fig. S5,† the characteristic peak of F 1s can be clearly observed, proving successful coverage of fluorine-containing TFs on CTFPNMs. Furthermore, Table S2† shows a noticeable change on the surface tensions of TFPNMs with different terminal groups, confirming that the TFs have been coated on CTFPNMs.


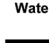








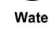

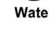

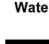

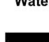




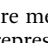
## 2.2 The wetting behaviors

The wetting behaviors of CTFPNM were evaluated by a contact angle meter. In Fig. 2a, a water droplet spread out and permeated into the membrane within 8 s, giving a contact angle (CA) of almost 0°. Analogous process occurred when an oil droplet (cyclohexane, CYH) was used as a detecting probe, and the permeation of oil droplet was completed within 7 s (Fig. 2b). Strikingly, when the CTFPNM was immersed in oil or water, the surface became dual superlyophobic with under-oil water contact angle ( $\theta_{w/o}$ ) of  $151.3 \pm 1.1^\circ$  or under-water oil contact angle ( $\theta_{o/w}$ ) of  $152.7 \pm 1.9^\circ$  (Fig. 2c and d). Fig. 2e and f show the  $\theta_{o/w}$  for a selection of oils and the corresponding  $\theta_{w/o}$ . All of them were above  $130^\circ$ , suggesting the extraordinary prewetting-

induced dual lyophobic property of the CTFPNM. Furthermore, the 4-cyan-Ph-terminated TF can protect the membrane from being corroded by aprotic solvents.<sup>34,44–46</sup> As shown in Fig. S6a and b,† the PNM were completely dissolved in dimethylformamide (DMF) and dimethyl sulfoxide (DMSO) within 5 min, whereas the CTFPNMs remained stable after soaking for 90 days (Fig. S6c and d†). Compared with the fresh-prepared membrane, no changes on both the morphologies and the under-liquid wetting behaviors were observed (Fig. S6e and f†), proving the outstanding stability of CTFPNM in organic solvents. It further confirms the successful grafting of the 4-cyan-Ph-terminated TF over PNM.

The under-liquid wetting behaviors of TFPNMs with other terminal groups were also measured in CYH–water–solid system. As seen in Table 1, these under-liquid wetting behaviors can be generally classified into three categories: (1) the under-water oleophobicity/under-oil hydrophilicity (plasma-treated CTFPNM, and 4-carboxyl-Ph-terminated TFPNM), (2) under-water oleophilicity/under-oil hydrophobicity (4-trifluoromethoxy-Ph-, 3-trifluoromethyl-Ph-, and naphthyl-

Table 1 The under-liquid wetting behaviors of TFPNMs with different terminal groups<sup>a</sup>

TFPNMs	$\theta_{o/w}^b (^\circ)$	$\theta_{w/o}^b (^\circ)$	
4-Trifluoromethoxy-Ph-TFPNM	$70.9 \pm 1.0$	$157.5 \pm 3.8$	 CYH  Water
Naphthyl-TFPNM	$70.8 \pm 1.1$	$155.2 \pm 3.7$	 CYH  Water
3-Trifluoromethyl-Ph-TFPNM	$85.2 \pm 1.2$	$150.9 \pm 3.5$	 CYH  Water
4-Fluoro-Ph-TFPNM	$138.3 \pm 1.8$	$147.9 \pm 2.6$	 CYH  Water
3-Fluoro-4-hydroxy-Ph-TFPNM	$146.3 \pm 2.1$	$147.5 \pm 2.4$	 CYH  Water
Phenyl-TFPNM	$147.3 \pm 2.2$	$142.7 \pm 1.9$	 CYH  Water
4-Nitro-Ph-TFPNM	$150.1 \pm 3.6$	$144.2 \pm 2.2$	 CYH  Water
4-Cyan-Ph-TFPNM	$152.7 \pm 1.9$	$151.3 \pm 1.1$	 CYH  Water
4-Hydroxy-Ph-TFPNM	$144.8 \pm 3.1$	$142.7 \pm 1.9$	 CYH  Water
Plasma-treated CTFPNM	$147.8 \pm 3.2$	$80.5 \pm 0.8$	 CYH  Water
4-Carboxyl-Ph-TFPNM	$157.4 \pm 3.6$	$63.4 \pm 0.8$	 CYH  Water

<sup>a</sup> The under-water liquid wetting behaviors of TFPNMs were measured in cyclohexane (CYH)–water–solid system. <sup>b</sup>  $\theta_{o/w}$  and  $\theta_{w/o}$  represent the under-water oil contact angle and the under-oil water contact angle, respectively.

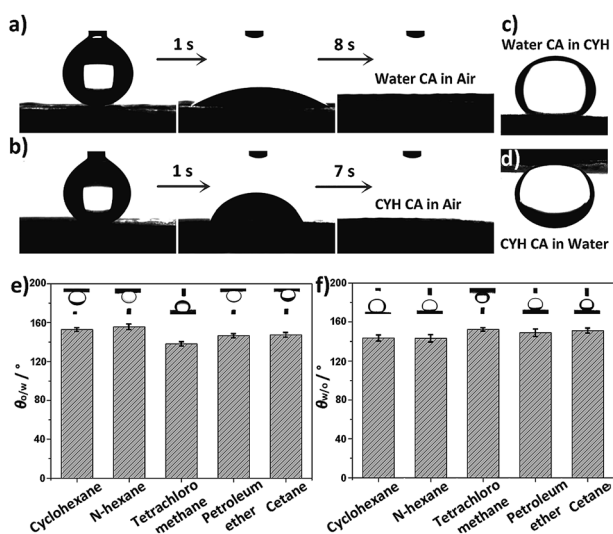


Fig. 2 The wetting behaviors of CTFPNM. (a and b) The permeation process of water and oil droplets into CTFPNM in air, respectively. (c and d) The  $\theta_{w/o}$  and the  $\theta_{o/w}$  of CTFPNM, respectively. During the measurement, the volume of the detecting droplet (water and CYH) was fixed at 3  $\mu$ L. (e and f) The  $\theta_{o/w}$  of CTFPNM for a selection of oils and the corresponding  $\theta_{w/o}$ , respectively. The selection of oils includes: cyclohexane, *n*-hexane, tetrachloromethane, petroleum ether and cetane. All the  $\theta_{o/w}$  and  $\theta_{w/o}$  are above  $130^\circ$ .



terminated TFPNMs), and (3) under-liquid dual lyophobicity (phenyl-, 4-hydroxy-Ph-TFPNM, 4-nitro-Ph-terminated TFPNMs, and CTFPNM, *etc.*). Because of the similar surface geometries of the TFPNMs with different terminal groups, the difference on the under-liquid wetting behaviors should be caused by the change of the surface chemical compositions, confirming the successful modification of TFs on the PNM. Herein, the representative CTFPNM was taken as an example to test the separation efficiencies of the under-liquid dual superlyophobic membranes for various oil/water mixtures.

### 2.3 The separation capacity of CTFPNM

To test the separation capacity of CTFPNM, conventional oil/water mixtures with oil density higher (*e.g.*, tetrachloromethane, TCM) or lower (*e.g.*, cyclohexane, CYH) than water, and the surfactant-stabilized oil-in-water (CYH/water) or water-in-oil (water/CYH) emulsions were prepared. For the separation of conventional oil/water mixtures, high density liquid (water in Fig. S7a† and TCM in Fig. S7b†) quickly passed through CTFPNM, and the low density liquid was retained. This was attributed to the under-water superoleophobicity and under-oil superhydrophobicity triggered by the prewetted water and TCM, respectively. Based on the under-liquid dual superlyophobicity of CTFPNM, the bi-continuous oil/water separation could be achieved by using a T-shape separation apparatus, the two outlets of which were fixed by water and CYH prewetted CTFPNMs, respectively. After the continuous separation for 1 h, no immiscible liquids were observed in the filtrates (Fig. S7c†). The oil and water fluxes of CTFPNMs reached to  $1078.35 \pm 6.41 \text{ L m}^{-2} \text{ h}^{-1}$  and  $974.74 \pm 6.08 \text{ L m}^{-2} \text{ h}^{-1}$ , respectively. The separation efficiencies for a series of oil/water mixtures were calculated by measuring the residual oil content and water content in the filtrates, respectively (Fig. S7d and e†). There was only a trace amount of residual oil or water existed in the collected liquids, and the separation efficiencies of CTFPNMs were all above 99.6%. We further prolonged the separation time to 10 h to test the stability of CTFPNM. The separation efficiencies kept stable and there was no visible attenuation during the separation process, proving the high stability of CTFPNM (Fig. S8†). Fig. 3 presents the separation of surfactant-stabilized CYH/water (flux rate:  $430.63 \pm 5.57 \text{ L m}^{-2} \text{ h}^{-1}$ ) and water/CYH (flux rate:  $606.72 \pm 5.79 \text{ L m}^{-2} \text{ h}^{-1}$ ) emulsions by water and CYH prewetted CTFPNMs, respectively. As seen that the micron-sized droplets dispersed evenly in both opaque emulsions. While after the filtration process, densely-packed droplets were completely removed and the milky emulsions became transparent. The above results demonstrate that the CTFPNM can realize the high efficient separation of all kinds of oil/water mixtures, even surfactant-stabilized emulsions.

### 2.4 The relationship between the under-liquid wetting behaviors and the intrinsic water contact angle

The under-liquid wetting behaviors of the as-prepared TFPNMs can be modulated by altering the terminal groups of the coated TFs, which cover the spectra of under-water oleophobicity/under-oil hydrophilicity, the under-water oleophilicity/under-

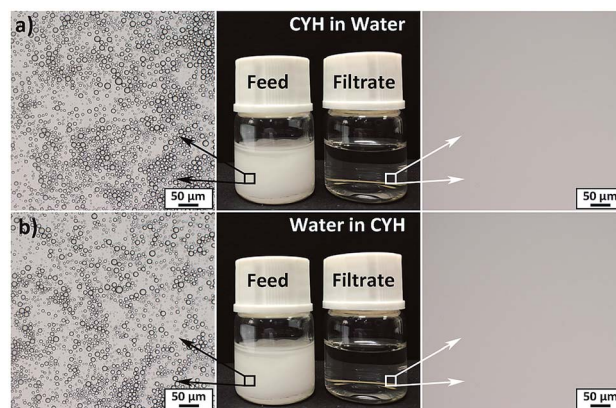


Fig. 3 The separation of surfactant stabilized emulsions by CTFPNM. (a) The separation of oil-in-water emulsion (CYH/water, stabilized by CTAB) by water-prewetted CTFPNM. (b) The separation of water-in-oil emulsion (water/CYH, stabilized by CTAB) by CYH-prewetted CTFPNM.

oil hydrophobicity, and the under-liquid dual lyophobicity. In order to investigate the influence of the surface chemical compositions on the wetting behaviors, we measured the intrinsic water contact angles ( $\theta_w$ ) on the smooth surfaces, which possessed the same chemical compositions as that of the corresponding TFPNMs (Table S3†). Combining with the results in Table 1, it is found that the under-liquid wetting behaviors of TFPNMs in CYH–water–solid system can be classified into three regions by using  $\theta_w$  as a variable (Fig. 4a): when the  $\theta_w$  is less than  $24.8^\circ \pm 0.9^\circ$ , the TFPNMs preferentially interact with water, showing under-oil hydrophilicity (as illustrated in Fig. 4b). In contrast, the TFPNMs exhibit under-water oleophilicity when the  $\theta_w$  is greater than  $93.8^\circ \pm 2.1^\circ$  (Fig. 4d). The under-liquid dual lyophobic TFPNMs are obtained with  $\theta_w$  ranging from  $52.2^\circ \pm 1.2^\circ$  to  $88.5^\circ \pm 1.9^\circ$  (Fig. 4c). Note that, there exists a shadow section with  $\theta_w$  values ranging from  $24.8^\circ$  to  $52.2^\circ$ , which is caused by the lack of suitable experimental modulations of TFPNMs.

### 2.5 The thermodynamic underlying nature of the under-liquid wetting behaviors

To explore the underlying nature of the under-liquid wetting behaviors of TFPNMs, we compared the total interfacial energies of two wetting models:<sup>47,48</sup> (1) surface infused by liquid A or liquid B with liquid A floating on it, (2) surface infused by liquid A and liquid B, respectively. The equations can be described as followings:

$$\Delta E_1 = R(\gamma_B \cos \theta_B - \gamma_A \cos \theta_A) - \gamma_{AB} \quad (1)$$

$$\Delta E_2 = R(\gamma_B \cos \theta_B - \gamma_A \cos \theta_A) + \gamma_A - \gamma_B \quad (2)$$

where  $\Delta E_1$  and  $\Delta E_2$  represent the total interfacial tensions of the wetting model 1 and wetting model 2, respectively (Fig. S9†).  $\theta_A$  and  $\gamma_A$ ,  $\theta_B$  and  $\gamma_B$  are the intrinsic contact angles on the smooth surfaces and surface tensions of the liquid to be repelled (liquid A) and the infused liquid (liquid B), respectively (Tables S3 and



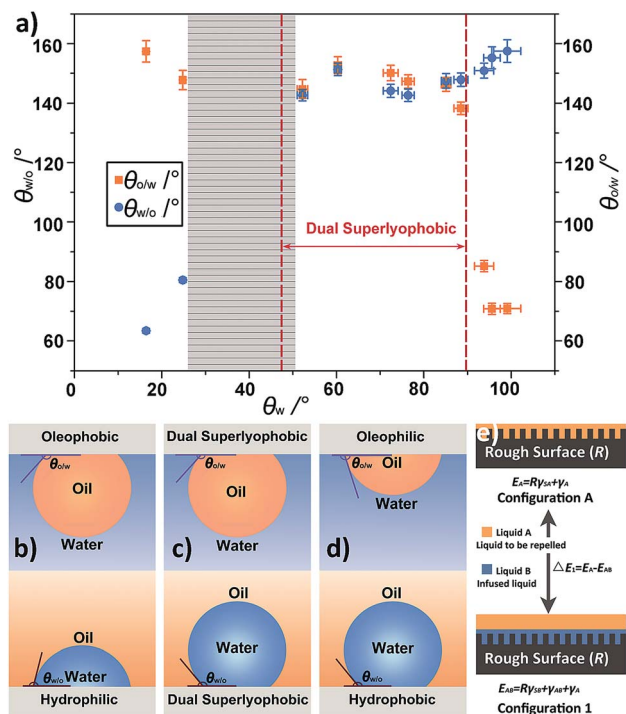


Fig. 4 The under-liquid wetting behaviors of TFPNMs. (a) In the CYH–water–solid system, the relationship between the  $\theta_w$  values and the under-liquid wetting behaviors of TFPNMs. The under-liquid wetting behaviors of TFPNMs can be divided into three regions by using the  $\theta_w$  as the variable, and the under-liquid dual lyophobic TFPNMs can be obtained with the  $\theta_w$  ranging from  $47.3^\circ$  to  $89.1^\circ$  (two dotted red lines). The shadow of  $\theta_w$  ranging from  $24.8^\circ$  to  $52.5^\circ$  is attributed to the lack of suitable experimental modulations of TFPNMs. (b, c and d) The illustrations of under-water oleophobic/under-oil hydrophilic surface, under-liquid dual lyophobic surface, and under-water oleophilic/under-oil hydrophobic surface, respectively. (e) Wetting model 1 of the surface infused by liquid A or liquid B with liquid A floating on it.

S6†).  $R$  is the roughness factor, defined as the ratio of the actual surface area to the projected surface area,<sup>35</sup> which is equal to 2 for TFPNMs due to their textured structure.<sup>48,49</sup>  $\gamma_{AB}$  represents the interfacial tension between liquid A and liquid B, which is measured by the pendant droplet method (Table S7†).<sup>50</sup> As for a thermodynamically stable surface that is preferentially wetted by liquid B or liquid A,  $\Delta E_1$  and  $\Delta E_2$  must simultaneously be greater or less than zero. In CYH–water–solid system, the calculated results of 4-trifluoromethoxy-Ph-, 3-trifluoromethyl-Ph-, and naphthyl-terminated TFPNMs show that the  $\Delta E_1$  and  $\Delta E_2$  are all greater than zero when the surfaces are infused by CYH, conversely, they are less than zero on the water infused surfaces (Table S3†). It means that these surfaces are more stable when infused by CYH and show the under-water oleophilicity/under-oil hydrophobicity. In addition,  $\Delta E_1$  and  $\Delta E_2$  are simultaneous greater and less than zero on the water and CYH infused surfaces (plasma-treated CTFPNM and 4-carboxyl-Ph-terminated TFPNMs), respectively, indicating they preferentially interact with water and exhibit the under-water oleophobicity/under-oil hydrophilicity. These results agree well with the experimental results (Table 1), which prove that

these surfaces are thermodynamically favorable. Although both  $\Delta E_1$  and  $\Delta E_2$  are less than zero on the water infused surfaces (phenyl-, 4-hydroxy-Ph-TFPNM, 4-nitro-Ph-terminated TFPNMs, and CTFPNM, etc.), they are opposite in sign when the surfaces are infused by CYH, that is, one positive one negative. This means that these formulas cannot identify whether the infused CYH can be substituted by water or not, suggesting that the wetting behaviors of these surfaces are conflicting in thermodynamics. Combining with the experimental results in Table 1, we can conclude that the under-liquid dual lyophobic surfaces are thermodynamically metastable.

Based on the above results, we propose a principle that can evaluate the under-liquid wetting behaviors of surfaces. The  $\theta_w$  regions corresponded to the three under-liquid wetting behaviors (Fig. 4b–d) can be predicted by calculating the boundary value of  $\theta_w$ . In wetting model 2 (Fig. S9†),  $\Delta E_2$  is the energy difference between the surface simply infused by liquid A and liquid B. In the CYH–water–solid system, when CYH represents liquid B (the infused liquid) and liquid A (the liquid to be repelled), respectively, the calculated  $\Delta E_2$  cannot be simultaneously greater or less than zero, in other word, their signs must be opposite. On this basis, the boundary value of  $\theta_w$  in CYH–water–solid system, where the transition of the surface from thermodynamically stable state to metastable state occurs, can be calculated in the case of  $\Delta E_1 = 0$ . Note that, the intrinsic oil contact angles ( $\theta_o$ ) on different TFPNMs are all less than  $5^\circ$  (Table S3†), thus the value of  $\cos \theta_o$  in eqn (1) can be approximatively equal to 1. In the wetting model 1 (Fig. 4e), when CYH represents the infused liquid (liquid B) and the liquid to be repelled (liquid A), the corresponding values of  $\theta_w$  are calculated to be  $89.1^\circ$  and  $47.3^\circ$  (two dotted red lines in Fig. 4a), respectively. It means that when  $\theta_w$  is larger than  $89.1^\circ$  or less than  $47.3^\circ$ , the surfaces exhibit under-water oleophilicity with both  $\Delta E_1$  and  $\Delta E_2$  greater than zero or under-oil hydrophilicity with both  $\Delta E_1$  and  $\Delta E_2$  less than zero, indicating these surfaces are thermodynamically stable. When  $\theta_w$  locates between  $47.3^\circ$  and  $89.1^\circ$ , the opposite signs of  $\Delta E_1$  and  $\Delta E_2$  suggest that these surfaces are metastable in thermodynamics, corresponding to under-liquid dual lyophobicity. In Fig. 4a, it can be seen that all the experimental results are in accord with the theoretical results, proving that this principle can describe the under-liquid wetting behaviors of TFPNMs. The  $\theta_w$  range of TFPNMs in TCM–water–solid system was also calculated on the basis of this principle (Tables S4 and S5†). It can be seen that the calculated results well accord with the experimental results, and the under-liquid dual lyophobic surfaces can be obtained when the  $\theta_w$  locates in  $42.6$ – $89.7^\circ$  (Fig. S10†).

To test the applicability of this principle for the description of under-liquid wetting behaviors of solid surfaces, the total interfacial energies of several surfaces with different geometries in CYH–water–solid system and TCM–water–solid system were calculated, respectively. Firstly, the TFs coated vertical aligned silicon nanowire arrays (TFSNWs) were prepared (Fig. S11†),<sup>51</sup> and their under-liquid wetting behaviors in different oil–water–solid systems were measured (Table S8†). Because of the same chemical compositions and surface roughness factor ( $R = 2$ )<sup>48</sup> of these substrates as that of the corresponding TFPNMs, the calculated  $\theta_w$  ranges of the surfaces with under-liquid dual lyophobicity were also  $47.3$ – $89.1^\circ$  in CYH–water–solid system



and 42.6–89.7° in TCM–water–solid system, respectively, which well covered the experimental data (Fig. S12†). Subsequently, several reported under-liquid dual lyophobic surfaces with known roughness factor were studied.<sup>28</sup> As shown in Table S9,† the calculated results reveal that whether in CYH–water–solid system or in TCM–water–solid system, the surface with roughness factor of 1.36 either coated by 3-cyanopropyltrichlorosilane (CPTS) or SU8 photoresist achieves the opposite signs of  $\Delta E_1$  and  $\Delta E_2$ , which further confirm the feasibility of our principle on the description of surfaces with regular geometry.

### 3. Conclusions

In summary, we systematically modulated the under-liquid wetting behaviors of the electrospun PAN nanofibrous membranes by altering the surface chemical compositions of the coated thin-film composites, and successfully fabricated membranes with different under-liquid wetting behaviors, including under-water oleophobicity/under-oil hydrophilicity, under-water oleophilicity/under-oil hydrophobicity, and under-liquid dual lyophobicity. Among them, the representative 4-cyan-Ph-terminated TFPNM (CTFPNM) exhibited high mechanical strength, excellent stability in organic solvent, and under-liquid dual superlyophobicity, which could achieve the efficient separation of arbitrary oil/water mixtures, even surfactant-stabilized oil-in-water and water-in-oil emulsions. The underlying nature of the under-liquid wetting behaviors was investigated by means of thermodynamic wetting models. The calculated results proved that the under-liquid dual lyophobic surfaces were thermodynamically metastable. Furthermore, when using the intrinsic water contact angle ( $\theta_w$ ) as a parameter, the under-liquid dual lyophobic surfaces could be predicted within a  $\theta_w$  range in a given oil–water–solid system. For instance, the identified  $\theta_w$  range in the CYH–water–solid system for the under-liquid dual lyophobic surfaces ( $R = 2$ ) is from 47.3° to 89.1°, which well covers the experimental results. Our work offers an insight into the nature of under-liquid wetting behaviors of surfaces, and proposes a design principle for the fabrication of under-liquid dual superlyophobic surfaces in terms of  $\theta_w$  values. The rational construction of under-liquid dual superlyophobic surfaces will bring more potential applications in various fields, such as phase-transfer catalysis, fuel purification and microfluidic devices.

## 4. Experimental

### 4.1 Fabrication of polyacrylonitrile nanofibrous membrane

The polyacrylonitrile nanofibrous membrane (PNM) was prepared *via* electrospinning technique. Typically, 1.2 g PAN was completely dissolved in 8.75 g DMF solution containing 0.5 g water at 50 °C. Then the as-prepared solution was loaded into a syringe coupled with a 17-gauge needle. Positive electrical potential was applied on the metallic needle and negative electrical potential was on an aluminum foil, which was cut into 3 cm × 3 cm piece. The electrospinning time and working distance were kept at 20 min and 15 cm, respectively.

### 4.2 Fabrication of silicon nanowire array

The silicon nanowire array (SNW) was fabricated by acid-etch process. Typically, the cleaned silicon wafers (1 cm × 1 cm) were immersed into 200 mL aqueous solutions containing HF (5 M) and AgNO<sub>3</sub> (0.02 M). After etching for 0.5 h at 50 °C, the silicon wafers were placed in dilute nitric acid for at least one hour to remove the excess Ag. Then the silicon wafers were orderly washed by deionized water and ethanol for several times and dried under a flow of nitrogen.

### 4.3 Fabrication of polyacrylonitrile coatings on the substrates

The polyacrylonitrile (PAN) coatings on silicon nanowire arrays and silicon wafer were prepared by a spin-coating method. Typically, 0.4 wt% PAN in DMF solution was dropped onto the substrate, and spin-coated with the rotate speed of 1750 rpm for 1 min.

### 4.4 Fabrication of 4-cyan-Ph-terminated thin-film composite on the substrates

The 4-cyan-Ph-terminated thin-film was fabricated on the PAN nanofibers, as well as the PAN coated silicon wafer and SNW, through a modification process in hydrazine derivatives and ethylene glycol solution. Typically, one piece of PNM (3 × 3 cm), or two pieces of as-prepared PAN coated SNWs (1 × 1 cm) or as-prepared PAN coated silicon wafers (1 × 1 cm) were placed in ethylene glycol solution (150 mL) containing 1,4-dicyanobenzene (0.50 g, 3.90 mmol) and hydrazine dihydrochloride (0.82 g, 7.81 mmol), and then the hydrazine hydrate (4 mL, 41.23 mmol) was added. The reaction was conducted at 130 °C under argon atmosphere for 5 h. The resulting light yellow membrane was cooled down to the room temperature and washed by water, subsequently dried at 60 °C overnight.

### 4.5 Fabrication of thin-film composites with different terminal groups on the substrates

The thin-film composites with other terminal groups were fabricated on the as-prepared 4-cyan-Ph-terminated substrates. The fabrication process was similar to that of 4-cyan-Ph-terminated substrates. The molar ratio of nitriles (3.90 mmol), hydrazine dihydrochloride (0.82 g, 7.81 mmol), and hydrazine hydrate (4 mL, 41.23 mmol) in the ethylene glycol (150 mL), the molar ratio was fixed at 1.00 : 2.00 : 10.57.

### 4.6 Plasma surface treatment of 4-cyan-Ph-terminated substrates

The plasma treatment on the as-prepared 4-cyan-Ph-terminated substrates was performed in a plasma system (PT-03-LF), with the gas flow of O<sub>2</sub> at 50 cm<sup>3</sup> min<sup>-1</sup>, and the forward RF target power at 100 W for 3 min.

### 4.7 Separation of oil/water mixtures

The oil/water mixtures were prepared by mixing water and oil (CYH, cetane, petroleum ether, *n*-hexane, and tetrachloromethane) with volume ratio of 1 : 1, respectively, and stirred at





room temperature for 6 h. The oil-in-water and water-in-oil emulsions were prepared by adding a certain amount of CTAB ( $4 \text{ mg mL}^{-1}$ ) to the mixtures of water and CYH with volume ratio of 100 : 1 and 1 : 100, respectively.

The CTFPNM was fixed between two flanges, and pretreated by water or oil according to the type of the high density liquid. Then the oil/water mixture was poured onto the membrane through a glass tube and the filtrate was collected in a jar. The driving force during the separation process was its own gravity. For the measurement of liquid flux, the intrusion pressure was constant by maintaining the height of the solutions above the membrane of 15 cm.

The bi-continuous oil/water separation process was achieved by a T-shape separation apparatus. Water and CYH pretreated CTFPNMs were fixed onto the two outlets of the separation apparatus, respectively, and the oil/water mixture was supplied by a peristaltic pump.

#### 4.8 Characterizations

The morphologies of the samples were recorded on scanning electron microscope (SEM, JEOL JEM-6700F) and transmission electron microscope (TEM, Tecnai G2 S-Twin F20). Fourier transform infrared spectrum (FT-IR) was recorded from 400 to  $4000 \text{ cm}^{-1}$  on a Nicolet Impact 410 FTIR spectrometer. X-ray photoelectron spectroscopy (XPS) was performed on an ESCA-LAB 250 spectrometer. The mechanical properties of the membranes were measured using a testing device 410R250 (TestResources, Shakopee, MN) and five samples were tested for each stack. The contact angles (CAs) were analyzed by an optical contact angle meter (DSA100, KRÜSS) at ambient conditions (temperature:  $23\text{--}25^\circ\text{C}$ ), and each value was obtained by measuring five different positions. Optical microscopy images were taken on a CMM-55E (Leica, Germany). The residual oil concentrations in water and water concentrations in oil were measured by infrared oil menstruation instrument (OIL-480) and trace moisture analyzer (HTYWS-H), respectively.

## Conflicts of interest

There are no conflicts to declare.

## Acknowledgements

We acknowledge the National Natural Science Foundation of China (Grant No. 21621001 and 21835002), the 111 Project (No. B17020) and the Jilin Province/Jilin University Co-construction Project-Funds for New Materials (SXGJSF2017-3) for supporting this work.

## Notes and references

- 1 K. Chen, S. Zhou and L. Wu, *ACS Nano*, 2016, **10**, 1386–1394.
- 2 L. Feng, W. Li, J. Ren and X. Qu, *Nano Res.*, 2014, **8**, 887–899.
- 3 S. K. Madhurakkat Perikamana, J. Lee, Y. B. Lee, Y. M. Shin, E. J. Lee, A. G. Mikos and H. Shin, *Biomacromolecules*, 2015, **16**, 2541–2555.
- 4 E. Ueda and P. A. Levkin, *Adv. Mater.*, 2013, **25**, 1234–1247.
- 5 S. Wang, K. Liu, X. Yao and L. Jiang, *Chem. Rev.*, 2015, **115**, 8230–8293.
- 6 Y. Fu, J. Jiang, Q. Zhang, X. Zhan and F. Chen, *J. Mater. Chem. A*, 2017, **5**, 275–284.
- 7 M. He, Y. Ding, J. Chen and Y. Song, *ACS Nano*, 2016, **10**, 9456–9462.
- 8 A. Das, S. Sengupta, J. Deka, A. M. Rather, K. Raidongia and U. Manna, *J. Mater. Chem. A*, 2018, **6**, 15993–16002.
- 9 X. Su, H. Li, X. Lai, L. Zhang, X. Liao, J. Wang, Z. Chen, J. He and X. Zeng, *ACS Appl. Mater. Interfaces*, 2018, **10**, 4213–4221.
- 10 M. Liu, S. Wang, Z. Wei, Y. Song and L. Jiang, *Adv. Mater.*, 2009, **21**, 665–669.
- 11 U. Manna and D. M. Lynn, *Adv. Funct. Mater.*, 2015, **25**, 1672–1681.
- 12 G. Caputo, B. Cortese, C. Nobile, M. Salerno, R. Cingolani, G. Gigli, P. D. Cozzoli and A. Athanassiou, *Adv. Funct. Mater.*, 2009, **19**, 1149–1157.
- 13 F. Gao, Y. Yao, W. Wang, X. Wang, L. Li, Q. Zhuang and S. Lin, *Macromolecules*, 2018, **51**, 2742–2749.
- 14 S. H. Anastasiadis, *Langmuir*, 2013, **29**, 9277–9290.
- 15 F. Xia, L. Feng, S. Wang, T. Sun, W. Song, W. Jiang and L. Jiang, *Adv. Mater.*, 2006, **18**, 432–436.
- 16 W. Zhang, N. Liu, Q. Zhang, R. Qu, Y. Liu, X. Li, Y. Wei, L. Feng and L. Jiang, *Angew. Chem., Int. Ed.*, 2018, **57**, 5740–5745.
- 17 G. Zhang, Z. Duan, Q. Wang, L. Li, W. Yao and C. Liu, *Appl. Surf. Sci.*, 2018, **427**, 628–635.
- 18 B. Wang, W. Liang, Z. Guo and W. Liu, *Chem. Soc. Rev.*, 2015, **44**, 336–361.
- 19 L. Wen, Y. Tian and L. Jiang, *Angew. Chem., Int. Ed.*, 2015, **54**, 2–15.
- 20 B. Xin and J. Hao, *Chem. Soc. Rev.*, 2010, **39**, 769–782.
- 21 J. Yong, F. Chen, Q. Yang, J. Huo and X. Hou, *Chem. Soc. Rev.*, 2017, **46**, 4168–4217.
- 22 J. Li, D. Li, Y. Yang, J. Li, F. Zha and Z. Lei, *Green Chem.*, 2016, **18**, 541–549.
- 23 N. Liu, X. Lin, W. Zhang, Y. Cao, Y. Chen, L. Feng and Y. Wei, *Sci. Rep.*, 2015, **5**, 9688.
- 24 M. Tao, L. Xue, F. Liu and L. Jiang, *Adv. Mater.*, 2014, **26**, 2943–2948.
- 25 C. L. Xu and Y. Z. Wang, *J. Mater. Chem. A*, 2018, **6**, 2935–2941.
- 26 W. Zhou, S. Li, Y. Liu, Z. Xu, S. Wei, G. Wang, J. Lian and Q. Jiang, *ACS Appl. Mater. Interfaces*, 2018, **10**, 9841–9848.
- 27 L. Cheng, D. M. Wang, A. R. Shaikh, L. F. Fang, S. Jeon, D. Saeki, L. Zhang, C. J. Liu and H. Matsuyama, *ACS Appl. Mater. Interfaces*, 2018, **10**, 30860–30870.
- 28 X. Tian, V. Jokinen, J. Li, J. Sainio and R. H. Ras, *Adv. Mater.*, 2016, **28**, 10652–10658.
- 29 A. B. D. Cassie and S. Baxter, *Trans. Faraday Soc.*, 1944, **40**, 546–550.
- 30 X. Zhou and C. He, *J. Mater. Chem. A*, 2018, **6**, 607–615.
- 31 H. Noh, J. M. Kim, H. Jo, H. S. Park, D. K. Hwang and M. H. Kim, *Int. J. Heat Mass Transfer*, 2018, **126**, 1315–1322.
- 32 S. Pan, R. Guo, M. Bjornmalm, J. J. Richardson, L. Li, C. Peng, N. Bertleff-Zieschang, W. Xu, J. Jiang and F. Caruso, *Nat. Mater.*, 2018, **17**, 1040–1047.



- 33 A. R. Bielinski, M. Boban, Y. He, E. Kazyak, D. H. Lee, C. Wang, A. Tuteja and N. P. Dasgupta, *ACS Nano*, 2017, **11**, 478–489.
- 34 J. W. Gose, K. Golovin, M. Boban, J. M. Mabry, A. Tuteja, M. Perlin and S. L. Ceccio, *J. Fluid Mech.*, 2018, **845**, 560–580.
- 35 G. Kwon, E. Post and A. Tuteja, *MRS Commun.*, 2015, **5**, 475–494.
- 36 C. Li, M. Boban, S. A. Snyder, S. P. R. Kobaku, G. Kwon, G. Mehta and A. Tuteja, *Adv. Funct. Mater.*, 2016, **26**, 6121–6131.
- 37 C. He, J. Liu, J. Li, F. Zhu and H. Zhao, *J. Membr. Sci.*, 2018, **560**, 30–37.
- 38 M. S. A. Rahaman, A. F. Ismail and A. Mustafa, *Polym. Degrad. Stab.*, 2007, **92**, 1421–1432.
- 39 W. Zhang, J. Liu and G. Wu, *Carbon*, 2003, **41**, 2805–2812.
- 40 L. Pérez-Manríquez, J. Aburabi'e, P. Neelakanda and K.-V. Peinemann, *React. Funct. Polym.*, 2015, **86**, 243–247.
- 41 T. D. Lu, B. Z. Chen, J. Wang, T. Z. Jia, X. L. Cao, Y. Wang, W. Xing, C. H. Lau and S. P. Sun, *J. Mater. Chem. A*, 2018, **6**, 15047–15056.
- 42 F. Bentiss, M. Lagrenée, M. Traisnel, B. Mernari and H. Elattari, *J. Heterocycl. Chem.*, 1999, **36**, 149–152.
- 43 X. Shen, J. Dai, Y. Liu, X. Liu and J. Zhu, *Polymer*, 2017, **122**, 258–269.
- 44 K. Vanherck, G. Koeckelberghs and I. F. J. Vankelecom, *Prog. Polym. Sci.*, 2013, **38**, 874–896.
- 45 I. B. Valtcheva, S. C. Kumbharkar, J. F. Kim, Y. Bhole and A. G. Livingston, *J. Membr. Sci.*, 2014, **457**, 62–72.
- 46 D. Chen, X. Liu, D. Li and X. Li, *RSC Adv.*, 2016, **6**, 29570–29575.
- 47 Y. Wang, J. Di, L. Wang, X. Li, N. Wang, B. Wang, Y. Tian, L. Jiang and J. Yu, *Nat. Commun.*, 2017, **8**, 575.
- 48 T. S. Wong, S. H. Kang, S. K. Tang, E. J. Smythe, B. D. Hatton, A. Grinthal and J. Aizenberg, *Nature*, 2011, **477**, 443–447.
- 49 D. Quéré, *Annu. Rev. Mater. Res.*, 2008, **38**, 71–99.
- 50 F. M. Fowkes, *Ind. Eng. Chem.*, 1964, **56**, 40–52.
- 51 B. Pokroy, A. K. Epstein, M. C. M. Persson-Gulda and J. Aizenberg, *Adv. Mater.*, 2009, **21**, 463–469.

